Ducting and Biases of GPS Radio Occultation Bending Angle and Refractivity in the Moist Lower Troposphere

Xuelei Feng[1*], Feiqin Xie[1], Chi O. Ao[2], and Richard A. Anthes[3]

1, Department of Physical and Environmental Sciences, Texas A&M University-Corpus Christi, Corpus Christi, TX, USA

2, Jet Propulsion Laboratory, California Institute of Technology, Pasadena, California, USA

3, COSMIC Program Office, University Corporation for Atmospheric Research, Boulder, Colorado, USA

Abstract

Radio occultation (RO) can provide high vertical resolution thermodynamic soundings of the planetary boundary layer (PBL). However, sharp moisture gradients and strong temperature inversion lead to large refractivity (*N*) gradients, and often cause ducting. Ducting results in systematically negative RO *N*-biases due to a non-unique Abel inversion problem. Using 8-year (2006-2013) Constellation Observing System for Meteorology Ionosphere and Climate (COSMIC) RO soundings and collocated European Centre for Medium-Range Weather Forecasts (ECMWF) interim reanalysis (ERA-I) data, we confirm that the large lower tropospheric negative *N*-biases are mainly located in the subtropical eastern oceans, and quantify the contribution of ducting for the first time. The ducting-contributed *N*-biases in the northeast Pacific (160°W~110°W; 15°N~45°N) are isolated from other sources of *N*-biases using a two-step geometric-optics simulation. Negative bending angle biases in this region are also observed in COSMIC RO soundings. Both the negative refractivity and bending angle biases from COSMIC soundings mainly lie below ~2-km. Such bending angle biases introduce additional *N*-biases to those caused by ducting. Following the increasing PBL height from the southern California coast westward to Hawaii, centers of maxima bending angles and *N*-biases tilt southwestward. In areas where ducting conditions prevail, ducting is the major cause of the RO *N*-biases. Ducting-induced *N*-biases with reference to ERA-I comprise over 70% of the total negative *N*-biases near the California coast where strongest ducting conditions prevail, and decrease southwestward to less than 20% near Hawaii.

1 Introduction

Since the proof-of-concept demonstration of the GPS/Meteorology experiment in 1995-1997 (Ware et al., 1996), many Global Positioning System (GPS) radio occultation (RO) satellite missions have been successfully deployed (e.g., Anthes et al., 2008, Anthes 2011). Radio occultation offers high-precision, high vertical resolution, and all-weather global sounding capability, which complement passive infrared and microwave sounders, and contribute to global weather forecasting and atmospheric research. Numerous studies quickly demonstrated the high-quality of RO data in the upper troposphere and lower stratosphere from GPS/MET (Rocken et al., 1997; Kursinski et al., 1997; Feng and Herman, 1999; Tsuda et al., 2000) and CHAMP (Wickert et al., 2001). However, these earlier RO missions equipped with phase-locked loop (PLL) tracking receivers encountered significant signal tracking challenges in the presence of large moisture variations in the lower troposphere. The complicated signal dynamics led to degraded RO signals and poorer data quality in the lower troposphere, such as systematic negative biases in bending angle and refractivity retrievals, along with low frequency of penetration into the lowest 1-2 km of the atmosphere (Ao et al., 2003; Beyerle et al., 2003; Sokolovskiy et al., 2003; Beyerle et al., 2006).

The implementation of open-loop tracking on the RO receivers allows high-quality RO signal tracking deep into the moist lower troposphere (Sokolovskiy et al., 2006; Ao et al., 2009). Over 80% of the retrieved profiles reach below 2-km altitude in the tropics, compared to only ~50% under closed-loop tracking (Ao et al., 2012). Nearly 85-90% of RO soundings reach below 1-km over the much drier Arctic Ocean (Yu et al., 2018). In addition, geometric-optics (GO) RO retrievals frequently encounter multipath problems in the presence of lower tropospheric moisture variations, which cause negative biases in the RO retrieved bending angle and refractivity profiles (Gorbunov and Gurvich, 1998). The introduction of the radio-holographic retrieval algorithms resolves the atmospheric multipath problems (Gorbunov, 2002a, 2002b; Sokolovskiy, 2003; Jensen et al., 2003; Jensen et al., 2004), and reduces RO biases in the moist lower troposphere. These techniques also overcome the limitation from Fresnel diffraction, and improve the vertical resolution up to ~ 60 m (Gorbunov et al., 2004).

Since 2006, the six-satellite Constellation Observing System for Meteorology, Ionosphere, and Climate (COSMIC), also known as the Formosa Satellite Mission 3 (FORMOSAT-3) in Taiwan, and the GNSS Receiver for Atmospheric Sounding (GRAS) on-board MetOp have produced over 3000 daily soundings globally (Anthes et al., 2008; Luntama et al., 2008). RO soundings are operationally assimilated into the numerical weather prediction (NWP) models at many weather forecast centers and have demonstrated positive impacts in the upper troposphere and lower stratosphere (UTLS) (Healy and Thépaut, 2006; Cucurull and Derber, 2008). RO observations have advanced knowledge of various physical processes, including the troposphere-stratosphere exchange, gravity waves, planetary boundary layer (PBL), and hurricane/typhoon evolution (Anthes, 2011, Bonafani et al. (2019), Ho et al. (2019), and references therein). Numerous studies have demonstrated the values of RO soundings in detecting the PBL height (e.g., Sokolovskiy et al., 2006; Sokolovskiy et al., 2007; Ao et al., 2008; Basha

and Ratnam, 2009; Guo et al., 2011; Ao et al., 2012; Xie et al., 2012). However, probing the PBL interior with RO remains challenging due to the existence of negative refractivity biases (a.k.a. *N*-biases) inside the moist PBL (Xie et al., 2010). The systematic *N*-biases are especially pronounced in the lower troposphere over the subtropical eastern oceans (Xie et al., 2010; Xie et al., 2012), where ducting is frequently observed (e.g., von Engeln and Teixeira, 2004; Lopez, 2009).

In the presence of ducting, it has been demonstrated that significant negative *N*-biases result from the non-unique inversion problem in the standard Abel inversion used to derive the RO refractivity retrieval from bending angles (Sokolovskiy, 2003; Ao et al., 2003; Xie et al., 2006; Ao, 2007). Theoretical explanations of the ducting induced *N*-biases from the standard Abel inversion can be found in Xie (2006) and Xie et al. (2006). It is worth noting that under the local spherically symmetric atmosphere assumption, the presence of ducting does not introduce biases in the RO bending angle when RO signals are perfectly recorded (Sokolovskiy, 2003).

Xie et al. (2010) found a major contribution of ducting to the RO *N*-biases in the lower troposphere. The large refractivity gradient associated with the ducting layer has a profound impact on the propagation of GPS radio signals and results in significant changes in both the phase and signal-to-noise-ratio (SNR) of the RO signals (Sokolovskiy, 2003), which may lead to bending angle errors and additional refractivity errors. The impact of signal tracking errors on the RO refractivity retrieval has been demonstrated in similar RO measurements from airborne platforms (Wang et al., 2016). To reduce refractivity biases due to ducting, additional information will be needed. A recent study showed that collocated precipitable water vapor retrieved from microwave radiometer measurements can be used in combination with the RO bending angle profiles to retrieve unbiased refractivity profiles in the presence of ducting (Wang et al., 2017).

In this paper, we analyse COSMIC RO bending angle and refractivity errors in reference to the European Centre for Medium-Range Weather Forecasts (ECMWF) Reanalysis Interim (ERA Interim, ERA-I) and in-situ radiosonde soundings with the focus on the northeast Pacific Ocean, where the Marine Atmospheric Radiation Measurement (ARM) GCSS Pacific Cross-section Intercomparison (GPCI) Investigation of Clouds (MAGIC) experiment was carried out (Zhou et al., 2015). The *N*-biases solely due to the standard Abel inversion problem in the presence of ducting in the ERA-I data are quantified, and the remaining *N*-biases due to other factors are also estimated. Section 2 presents data and methodology used for this study. The global distributions of ducting frequency from the reanalysis, and the PBL refractivity and *N*-biases from COSMIC RO soundings are described in Section 3. Section 4 details the mean bending angle and *N*-biases over the northeast Pacific Ocean, and further estimates the fraction of *N*-biases resulting from the standard Abel-retrieval in the presence of ducting in the ERA-I data. Section 5 summarizes the results and conclusions.

2 Data and Methodology

2.1 Data Description

The COSMIC level-2 refractivity and bending angle data are obtained from UCAR CDAAC (https://cdaac-www.cosmic.ucar.edu/). The retrieval procedures are described in Kuo et al. (2004). The refractivity retrieval is reported as a function of geometric height above mean-sea-level (MSL), and the bending angle is reported as a function of impact parameter, which is the product of refractive index and radius at the tangent point. Although RO soundings could theoretically achieve ~60-m vertical resolution (Goburnov, 2004; Zeng et al., 2019), the resolution of RO bending angle and refractivity profiles in the lower troposphere is limited by a 200-m filter applied in the standard retrieval (Ho et al., 2009) to reduce measurement noise.

Six-hourly air temperature (*T*), pressure (*P*), and specific humidity (*q*) from ERA-I are used. The ERA-I archive is a global atmospheric reanalysis from 1979 (Dee et al., 2011). It has a spectral resolution of T255, with a horizontal grid of ~0.75° latitude × 0.75° longitude (~80-km near the equator), on 60 vertical levels from the surface up to 0.1 hPa-pressure level. There are about 14 unevenly-spaced layers below 2-km (~800 hPa), with denser sampling near the surface. The vertical resolution is ~200-m between 900 and 800 hPa, decreasing to ~30-m near the surface. ERA-I assimilates COSMIC RO bending angles (Healy, 2008), but it doesn't assimilate bending angles below the ducting layer, which generally occurs near the PBL top (Poli et al., 2010). Because ducting occurs frequently over the subtropical eastern oceans, including the northeast Pacific Ocean (von Engeln and Teixeira, 2004; Lopez, 2009), the RO and the reanalysis data can be considered mostly independent inside the PBL in these regions. For each COSMIC profile, the closest collocated ERA-I profile within 3 hours in time and less than ~40-km in space (e.g., within 0.375°, or half-size of an ERA-I grid) over the northeast Pacific Ocean (160°W~110°W; 15°N~45°N) was identified. A total of 152,249 collocated pairs over this region were analyzed.

Furthermore, ship-borne radiosonde measurements from the MAGIC experiment are used. The refractivity profiles can be easily calculated from the radiosonde temperature (*T*), pressure (*P*), and relative humidity (*RH*) measurements. The MAGIC field campaign implemented the U.S. Department of Energy (DOE) Atmospheric Radiation Measurement Program Mobile Facility 2 (AMF2) on the commercial cargo container ship Horizon *Spirit* (Kalmus et al., 2015). The ship traveled back and forth along a near straight-line between Los Angeles, California and Honolulu, Hawaii from September 26, 2012 to October 2, 2013 (Zheng and Rosenfeld, 2015). Radiosondes were launched every six hours initially, but were launched every three hours after July 2013 (Zhou et al., 2015). A total of 583 radiosonde soundings were obtained. For each MAGIC radiosonde profile, the closest collocated COSMIC RO profile (if available) is identified within 3 hours and ~3º. The larger distance collocation criterion for radiosonde allows more collocated profiles (177 pairs) to be found.

2.2 Bending angle and refractivity simulation in the presence of ducting

In the neutral atmosphere, the refractivity, N, a dimensionless quantity defined as $N = (n - 1) \times 10^6$, where n is the refractive index, is related to the atmospheric pressure (P in hPa), temperature (T in Kelvins), and water vapor partial pressure (P_w in hPa) through (Smith and Weintraub 1953)

$$N = 77.6\frac{P}{T} + 3.73 \times 10^5 \frac{P_w}{T^2}. \quad (1)$$

Under the assumption of a local spherically symmetric atmosphere, a ray satisfies Bouguer's law, i.e., the impact parameter [$a = rn(r)sin\varphi$] is a constant for a given ray in the geometrical optics approximation, where r is the distance from the center of curvature, φ is the angle between the ray path and the radial direction (Born and Wolf 1964). The total refractive bending angle, α, as a function of r_t (i.e., the radius of the ray at the tangent point), is given by Fjeldbo et al. (1971) in (2), which can be further simplified to (3) given that $a(r)$ is a monotonic function and using the substitution $x = n(r)r$.

$$\alpha(a) = -2a \int_{r_t}^{\infty} \frac{1}{n}\frac{dn}{dr}\frac{dr}{\sqrt{(nr)^2 - a^2}}, \quad (2)$$

$$= -2a \int_{a}^{\infty} \frac{1}{n}\frac{dn}{dx}\frac{dx}{\sqrt{x^2 - a^2}}. \quad (3)$$

In the presence of a ducting layer, the impact parameter (a) is no longer a monotonic function of (r) inside and right below the ducting layer (e.g., Xie et al., 2006). Equation (2) instead of (3) is needed for calculating α. A detailed description of the special treatment of solving (2) in the presence of ducting layer can be found in Xie et al., (2006). Given a bending angle profile, the refractive index $n(r)$, is then solved for by inverting (3) through the Abel inversion (Fjeldbo et al. 1971)

$$n(r) = \exp\left[\frac{1}{\pi}\int_a^{\infty} \frac{\alpha(x)dx}{\sqrt{x^2 - a^2}}\right]. \quad (4)$$

Using the MAGIC radiosonde and ERA-I refractivity profiles calculated from (1), a simple two-step end-to-end geometric-optics (GO) simulation can be conducted. First, a forward operator is used to simulate the RO bending angle measurement by integrating an input refractivity profile (Eqs. 2 or 3). Second, an inverse operator is used to simulate the RO refractivity retrieval process by integrating the simulated bending angle profile through the standard Abel integration. The two GO operators that are specifically built for simulating ducting cases are described in Xie (2006) and Xie et al. (2006). In the absence of ducting, the Abel-retrieved refractivity profile will be identical to the input refractivity profile. However, in the presence of a duct, the Abel-retrieved refractivity profile becomes negatively biased inside the PBL. The percentage of ducting-induced N-biases can therefore be isolated and quantified as $(N_{\_retrieval} - N_{\_input})/N_{\_input} \times 100\%$.

3 Ducting climatology and the *N*-biases in RO soundings

An atmospheric duct is a horizontal layer in the lower atmosphere in which the vertical refractivity gradient is less than a critical value of -157 *N*-unit/km, such that radio signals are guided or ducted to follow the Earth's curvature (Thomas, 2006). The sharp refractivity gradient is generally caused by a coexisting sharp temperature inversion and negative moisture gradient across the top of the PBL. Here we analyzed ERA-I refractivity profiles from 2006 to 2013. The refractivity gradient profile is calculated at the model levels. A profile with ducting is identified when the minimum refractivity gradient is less than the critical value of -157 *N*-unit/km.

The 8-year mean annual ducting occurrence frequency is shown in Fig. 1a. The ducting frequency related figures (Fig. 1a and Fig. 3) are displayed at the model grids. This annual mean ducting frequency pattern is highly consistent with the results in Lopez (2009). The regions with high ducting frequency are clustered over the subtropical eastern oceans, where strong subsidence in the free troposphere along with the cool sea surface temperature results in strong temperature inversion. The sharp moisture gradient beneath the temperature inversion leads to large refractivity gradient, and often causes ducting across the PBL top (Xie et al., 2010). Six centers of high ducting frequency occur over the subtropical oceans off the west coast of continents, including North/South America, North/South Africa, and India/Australia, with the maximum ducting frequency exceeding 90%. Over the polar regions, including the Arctic, and the Antarctic Circumpolar Current areas, ducting is rarely observed.

The annual mean COSMIC refractivity at 1-km above surface is exhibited in Fig. 1b, which is similar to that of ERA-I (not shown). Note this mean COSMIC refractivity panel (Fig. 1b), as well as *N*-biases related figures in Section 3 (Figs. 1c, 1d, 2 and 4), is binned and displayed at the 3° latitude x 3° longitude grids. The refractivity maxima are centered on the tropical deep convective regions. Besides the polar regions, minimum refractivity values are also seen over high topography areas, such as Tibet Plateau, Andes, west coast of the U.S., and Greenland due to the relatively lower surface pressure, and the drier and cooler near-surface conditions. Minimum refractivity values also exist in the subtropical and mid-latitude deserts, such as Sahara and the Kalahari in Africa, Atacama and Patagonian in South America, western Australia, Gobi, Taklamakan, and Arabian deserts.

By differencing each COSMIC refractivity profile with its collocated ERA-I profile, the fractional RO refractivity error profile in reference to ERA-I can be estimated. Note the refractivity profiles from both COSMIC and ERA-I are interpolated to a 100-m grid before the differencing. The 8-year annual mean *N*-bias maps at 1-km and 2-km above the surface are shown in Fig. 1(c, d). Similar to Xie et al. (2012), large lower tropospheric *N*-biases are confined over the low latitudes (30°S-30°N, excluding the ITCZ/SPCZ), but are absent in higher latitudes. At the 1-km level (Fig. 1c), the *N*-biases are mostly clustered over the subtropical eastern oceans, which are characterized with high ducting frequency as seen in Fig. 1a. Over land, there are also large *N*-biases over the complex topography regions, such as Andes, Himalaya Mountains and central Africa. The maximum negative *N*-biases over the oceans can reach ~6%. It is important to note that these estimated *N*-biases could be affected by biases in the ERA-I reanalysis as well as

232 the RO retrievals. For example, Ho et al. (2015) found a low-bias in the ERA-I PBL
233 height of about 300-m off the coast of South America, a region with frequent ducting.
234 However, comparison of collocated refractivity profiles between ERA-I and MAGIC
235 radiosondes shows very small ERA-I *N*-biases (not shown). In the rest of this study, we
236 assume that the ERA-I reanalysis is accurate enough to represent the refractivity of the
237 real atmosphere.

238 As pointed out by Xie et al. (2010), the highly consistent pattern between the *N*-biases at
239 1-km and ducting frequency over the subtropical oceans strongly supports the importance
240 of ducting in producing the negative *N*-biases in the lowermost troposphere. The *N*-biases
241 over land, however, do not appear to be related to ducting, and will require further
242 investigation. Interestingly, the high frequency of ducting in the Antarctic region is also
243 not reflected in the *N*-biases panel (Fig. 1c). That is likely due to the limited GPS RO
244 sounding penetration and vertical resolution (~200 m), which might not be able to
245 identify the very shallow near-surface ducting layer over polar regions (Yu et al., 2018).

246 The negative *N*-biases at 1-km (Fig. 1c) become negligible or positive at the 2-km level
247 (Fig. 1d), except over several small land regions where negative biases remain. These
248 positive *N*-biases are primarily distributed in the tropical oceans including the tropical
249 Indian Ocean, western Pacific, central Pacific off the equator, and western Atlantic
250 Ocean. They have also been reported by several other studies (Ao et al., 2003; Beyerle et
251 al., 2006; Sokolovskiy at al., 2010; and Xie et al., 2010). Sokolovskiy et al. (2010)
252 showed that random noise associated with small-scale variations of lower tropospheric
253 water vapor coupled with a decrease of the truncation height of the RO signal in the
254 retrieval could cause a positive bias because of the asymmetry of the local spectrum of
255 noise of the RO signal. As the positive *N*-biases are not the emphasis of this study, we
256 focus our study on the negative biases in the lower level.

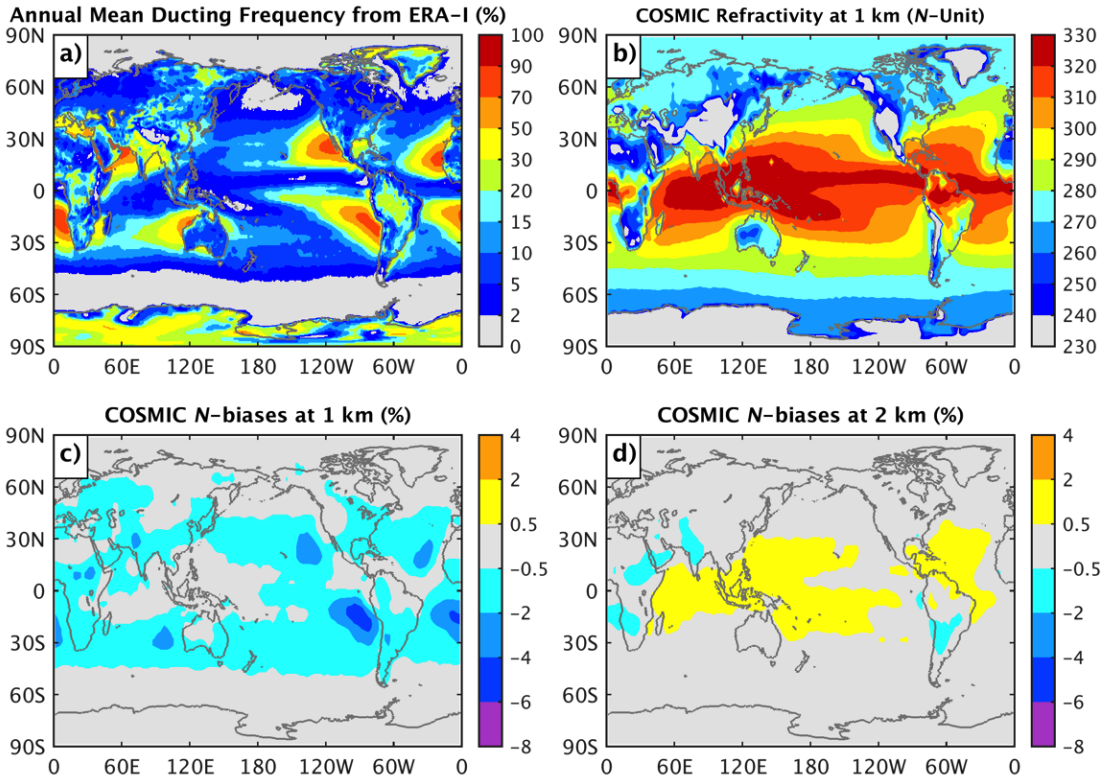

Figure 1. (a) Annual mean (2006~2013) ducting frequency from ERA-I, (b) Annual mean COSMIC refractivity (*N*) at 1-km, (c) the fractional COSMIC refractivity biases with respect to collocated ERA-I (c) at 1-km, and (d) at 2-km level. The COSMIC fractional *N*-bias is defined as $<(N_{COSMIC}-N_{ERAI})/N_{ERAI}>*100$ (%), where < > denotes the sample mean. Ducting frequency in (a) is defined as the percentage of soundings with ducting at any level to the total refractivity profiles in ERA-I. The values in (b), (c), and (d) are displayed at altitudes above the surface, which were converted from the height above MSL using high-resolution terrain data.

The seasonal variation of the ducting frequency derived from the ERA-I reanalysis is evident in Fig. 2, which is consistent with the ECMWF operational analysis (Lopez, 2009). The ducting events occur more often over ocean than over land, but the seasonality over land is stronger than that over ocean. Oceanic ducting prevails in the subtropics, with the maximum frequency clustering over the eastern oceans offshore of the western continents. The high-frequency region expands a little westward over the oceans in boreal autumn (September-November, SON; Fig. 2d) and winter (December-February, DJF; Fig. 2a) compared to spring (March-May, MAM; Fig. 2b) and summer (Jun-August, JJA; Fig. 2c). The North Indian Ocean has its highest frequency in MAM and the lowest in JJA, while the Mediterranean Sea reaches the maximum in JJA. Over land, high-frequencies of ducting center around the Amazon in JJA and SON, over Antarctica in MAM and JJA, and over Russia and Greenland in DJF.

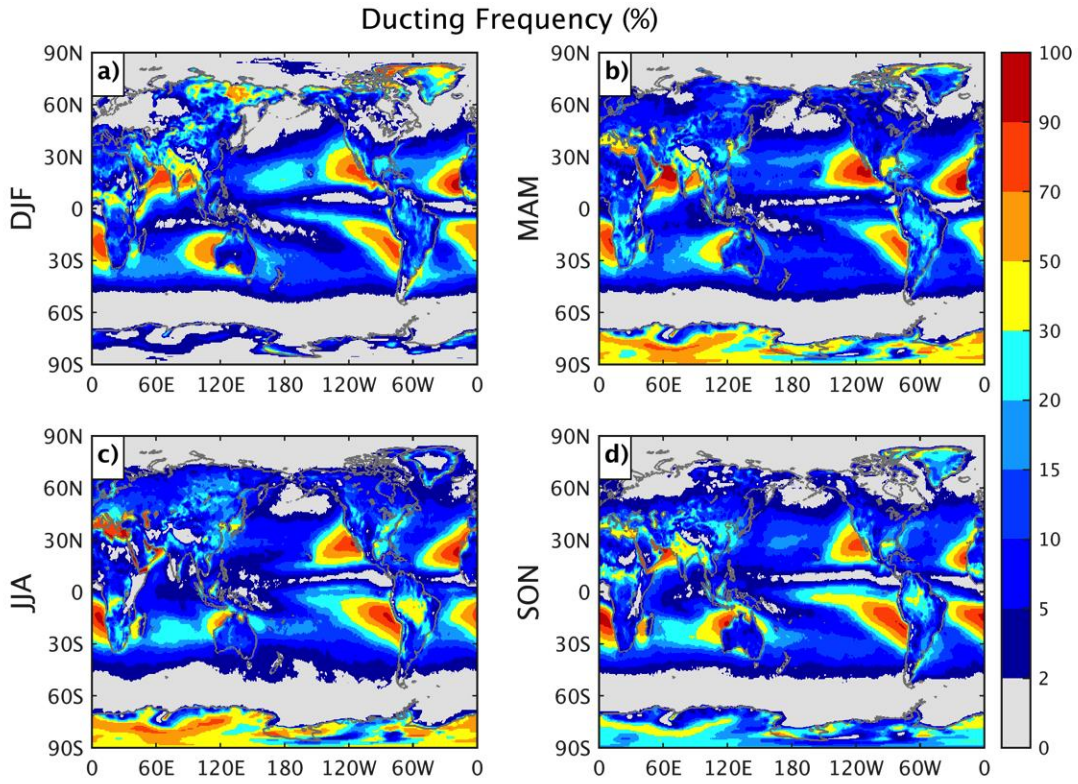

Figure 2. Seasonal-mean ducting frequency (%) from ERA-I in (a) DJF, (b) MAM, (c) JJA, and (d) SON, respectively. The values pertain to any layer in ERA-I with ducting.

The seasonal mean COSMIC fractional *N*-biases in comparison to the ERA-I at 1-km above the surface is shown in Fig. 3. The *N*-bias distributions in the DJF and JJA are qualitatively consistent with the corresponding panels in Fig.1 of Xie et al. (2010). The large biases are confined to the subtropical eastern oceans in MAM (Fig. 3b) and JJA (Fig. 3c), and extend far westward, almost covering the entire subtropical oceans in DJF (Fig. 3a) and SON (Fig. 3d). Moreover, significant negative *N*-biases only emerge over the Arctic in JJA. Over land, *N*-biases in central Africa areas are present in all seasons, albeit with seasonal variations in magnitude.

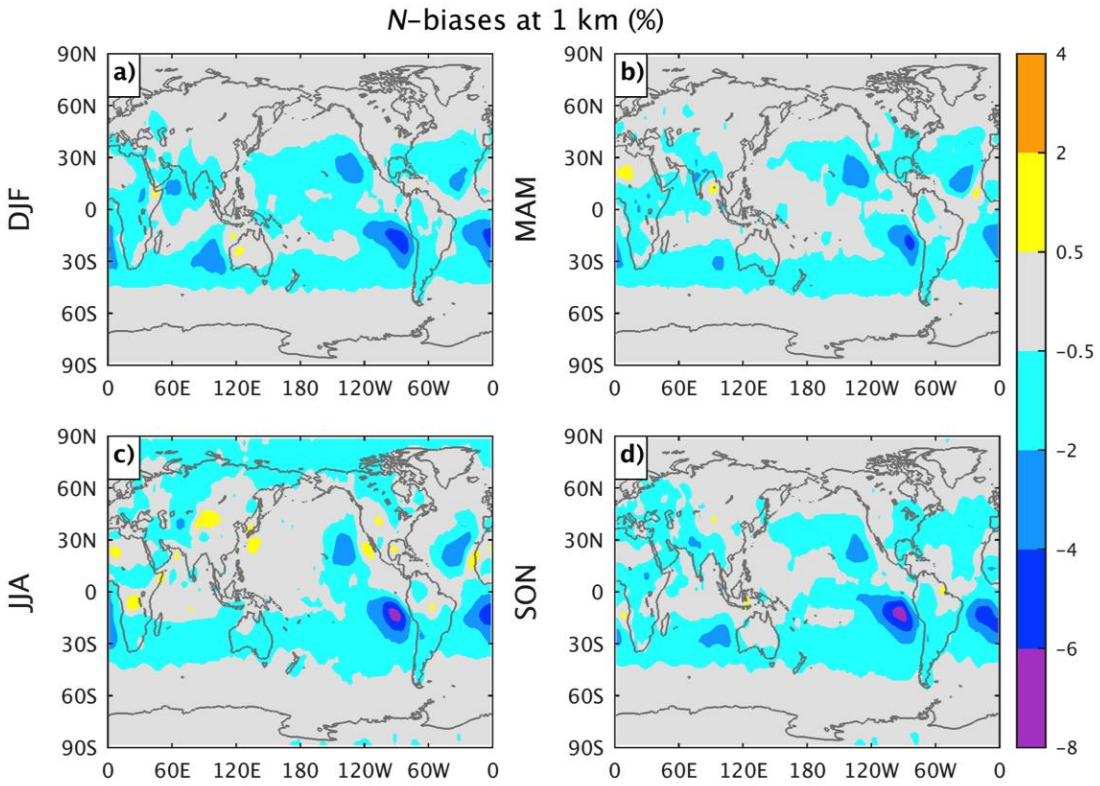

Figure 3. Seasonal mean fractional refractivity difference (*N*-biases) between COSMIC RO and collocated ERA-I at 1-km above the surface in (a) DJF, (b) MAM, (c) JJA, and (d) SON, respectively.

The systematic negative *N*-bias in COSMIC soundings due to the presence of ducting has been demonstrated in both observational and simulation studies (Sokolovskiy 2003, Xie et al., 2006, Ao 2007, Xie et al., 2010). However, a full quantitative assessment of the *N*-biases attributable to ducting and other factors has not been done. Figure 1c shows the total COSMIC RO *N*-biases in comparison to the collocated ERA-I. Here, the COSMIC RO profiles are separated into two groups: the first group consists of RO profiles for which the collocated ERA-I refractivity profiles show the presence of ducting, and the second group consists of RO profiles for which ducting is not present in collocated ERA-I profiles.

The annual mean COSMIC RO *N*-biases in the presence of ducting (in ERA-I) at 1-km above the surface are displayed in Fig. 4a. The overall distribution of *N*-bias is rather consistent with the total *N*-bias shown in Fig. 1c, but with much larger magnitudes. Systematic negative *N*-biases also exist in the non-ducting conditions (Fig. 4b), with similar pattern, but weaker in magnitude than those with ducting (Fig. 4a). The fractional negative *N*-bias under ducting conditions (Fig. 4a) can reach about 10% in magnitude, while the maximum in the non-ducting case (Fig. 4b) is only about 3%. The existence of significant *N*-biases in the non-ducting situations suggests that factors other than ducting contribute to the negative biases. Additional evidence for *N*-biases from non-ducting

factors will be demonstrated with bending angle errors in Section 4. Underestimation of ducting frequency in the ERA-I analysis could be another reason. The relatively coarse vertical resolution of ERA-I might fail to resolve strong vertical temperature and water vapor gradients in the real atmosphere.

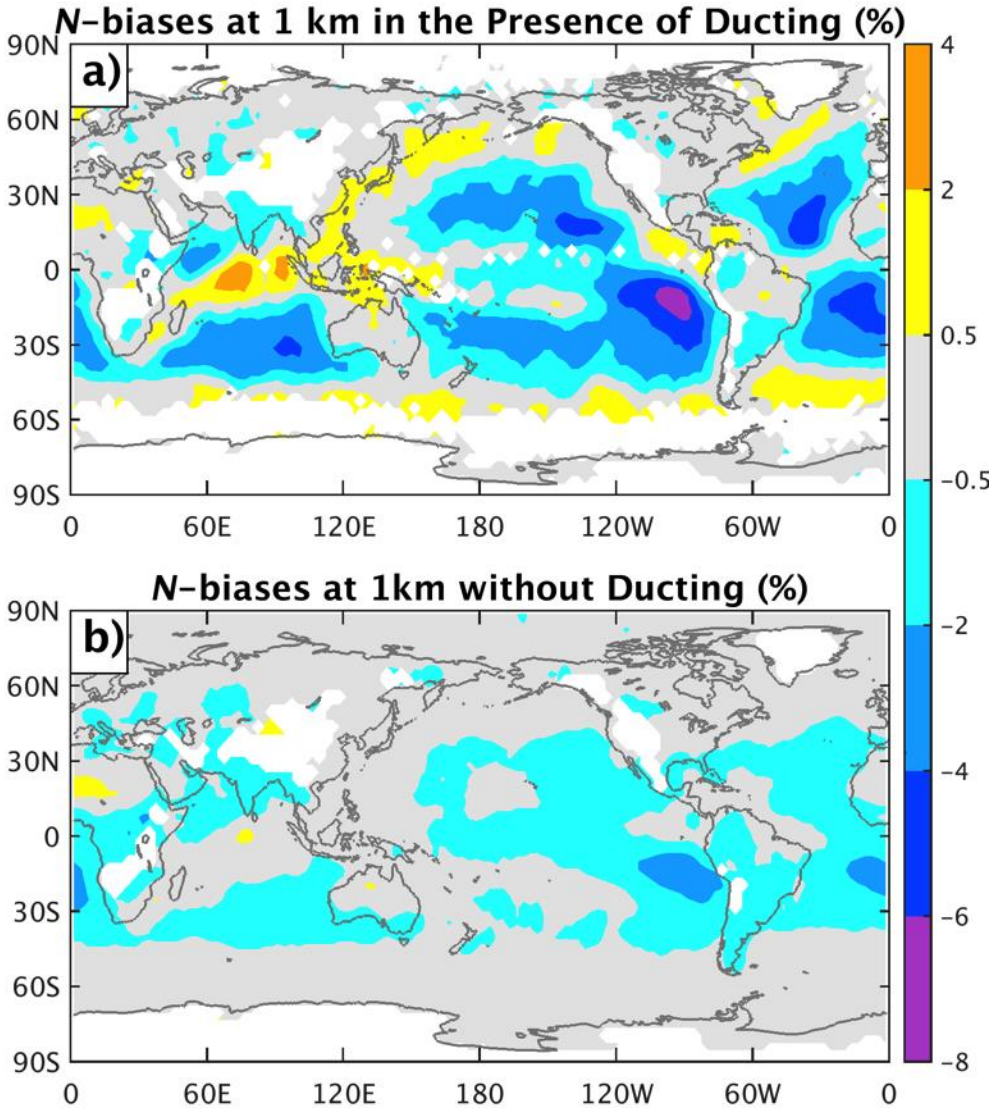

Figure 4. (a) COSMIC N-bias $<(N_{COSMIC}-N_{ERAI})/N_{ERAI}>*100$ (%) at 1-km above surface in the presence of ducting, and (b) in the absence of ducting as indicated by the collocated ERA-I profiles.

4 Retrieval errors of COSMIC soundings over the subtropical Northeast Pacific

In this section, we evaluate the refractivity and bending angle biases of COSMIC RO soundings against the collocated ERA-I reanalysis over the subtropical Northeast Pacific, where the MAGIC field campaign was carried out. MAGIC radiosonde profiles are also used to confirm the existence of bending angle biases.

4.1 COSMIC bending angle biases compared to MAGIC and ERA-I

Low-level *N*-biases in RO can be introduced by bending angle errors. Through the forward Abel expressions (Eqs. 2 and 3), the simulated bending angles of the reference data (e.g., ERA-I or radiosonde) can be computed. The COSMIC RO bending angle errors can be estimated by comparing the collocated RO bending angles with the simulated reference bending angles. The reference refractivity profiles are interpolated to a 10-m grid for calculating the bending angles.

We found a total of 177 collocated COSMIC and MAGIC radiosonde pairs. For consistency, the COSMIC and collocated ERA-I profiles over a quadrangle area [(158°W, 21°N), (158°W, 23°N), (118°W, 35.5°N), (118°W, 33.5°N)] (outlined in Fig. 6 with red lines), roughly coinciding with the MAGIC ship tracks during the campaign period (09/26/2012-10/02/2013), were identified. We also found a total of 911 collocated COSMIC and ERA-I pairs.

The mean COSMIC bending angle profiles along with the collocated MAGIC and ERA-I simulated bending angles are shown in Fig. (5a, b). The high-resolution input radiosonde refractivity profiles could result in significant fine-scale noise in the simulated MAGIC bending angles. Therefore the MAGIC refractivity profiles were smoothed with a 100-m moving average before calculating the bending angles. In order to remove high frequency noise, the simulated bending profiles are further vertically smoothed by a moving average of 50-m.

In Fig. 5, negative COSMIC bending biases occur below 2-km, while the biases above 2-km are negligible. The peak bending angle bias as large as ~10% occurs at ~1-km, where the maximum COSMIC bending angle reaches ~0.028 rad, and the maximum ERA-I and MAGIC values reach ~0.032 rad. The altitude of the peak bending angle in COSMIC is several hundred meters lower than those in the MAGIC and ERA-I profiles.

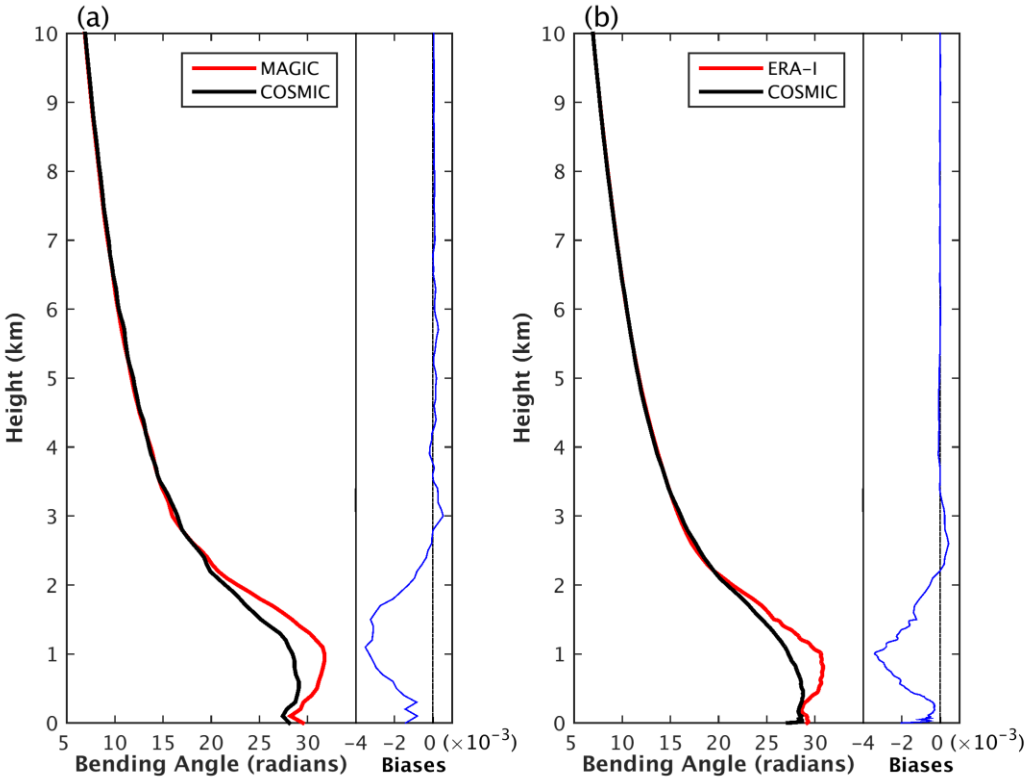

Figure 5. (a) The mean bending angle profiles for collocated COSMIC (black) and MAGIC radiosonde (red) (within 3 h and 3°). (b) The mean bending angle profiles for collocated COSMIC (black) and ERA-I (red) (within 3 h and 0.375°) roughly coinciding with the MAGIC ship tracks. Their bending angle bias profiles are displayed in the right side of the corresponding panels with blue lines.

4.2 COSMIC biases over the subtropical northeast Pacific

In this section, we expand the study region beyond the MAGIC transect to the northeast Pacific from southern California to Hawaii (160°W~110°W; 15°N~45°N) and compared COSMIC RO soundings and the ERA-I profiles over the period of 04/21/2006-12/31/2013. The collocated data are binned into 2° latitude × 2° longitude grids in this subsection.

Systematically negative COSMIC bending angle biases with reference to ERA-I bending angles (Fig. 6) are shown at all four altitudes (0.5, 1.0, 1.5 and1.8-km above MSL). At 0.5-km, the large bending angle biases are confined to the ocean off the west coast of southern California. With increasing altitude, the bias center moves southwestward toward Hawaii, but covers less area. The mean peak bending angle bias, with the magnitude of ~ -0.008 rad, occurs at 1-km, consistent with the results in Fig. 5b. From the MAGIC PBLH reference data, the PBL height increases from around 0.8-km near the California coast to ~1.8-km near Hawaii. Thus the location of the maximum bending angle biases at each altitude follows the location of peak bending angle and the PBL height.

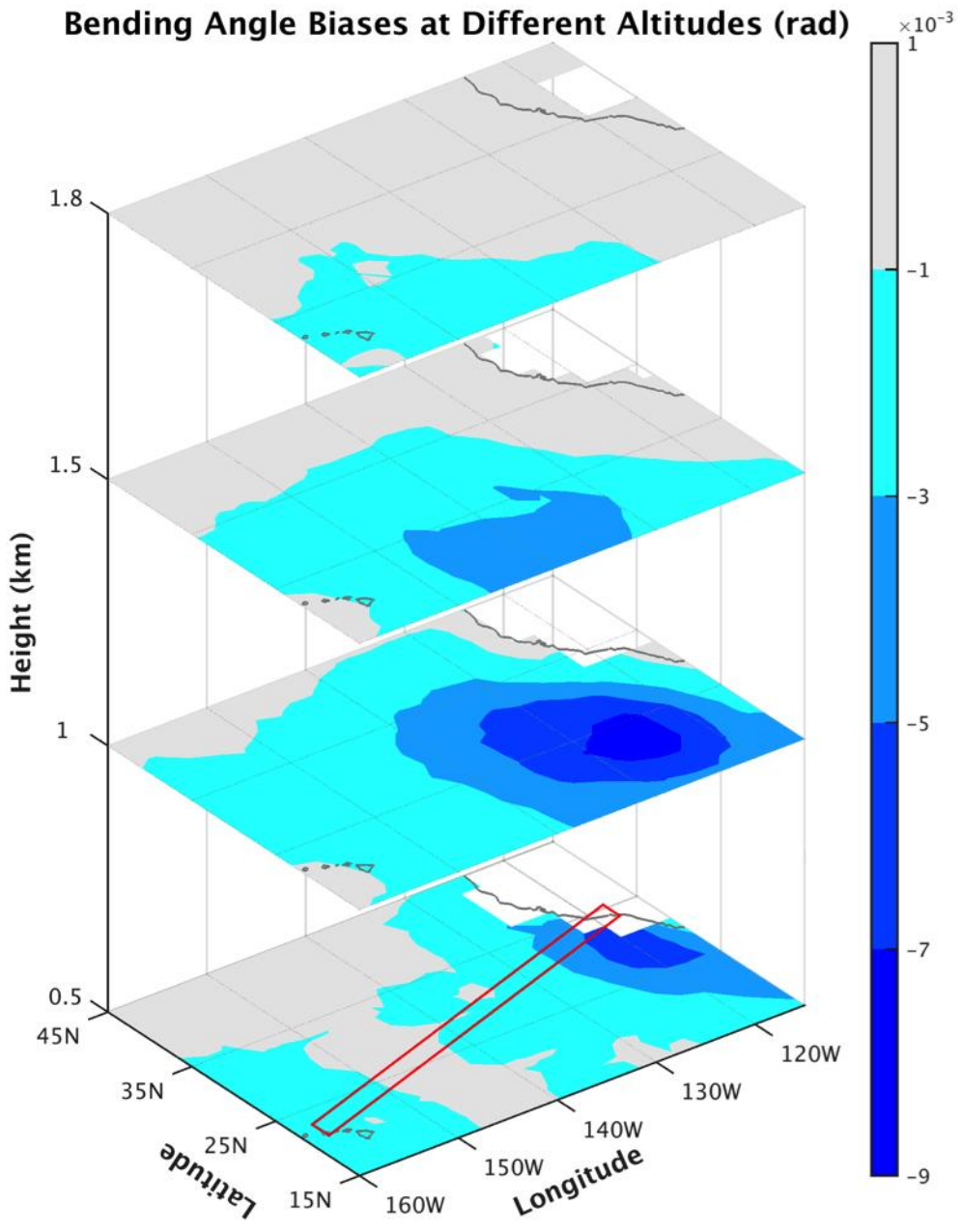

374

375 Figure 6. COSMIC RO bending angle biases with respect to the ERA-I $<(\alpha_{COSMIC} - \alpha_{ERAI})>$
376 (rad) at 0.5-km, 1.0-km, 1.5-km, and 1.8-km above mean sea level. Red lines outline the area
377 where the bending angle profiles of COSMIC and ERA-I are collocated for Fig. 5b. This area
378 roughly coincides with the MAGIC ship tracks.

379

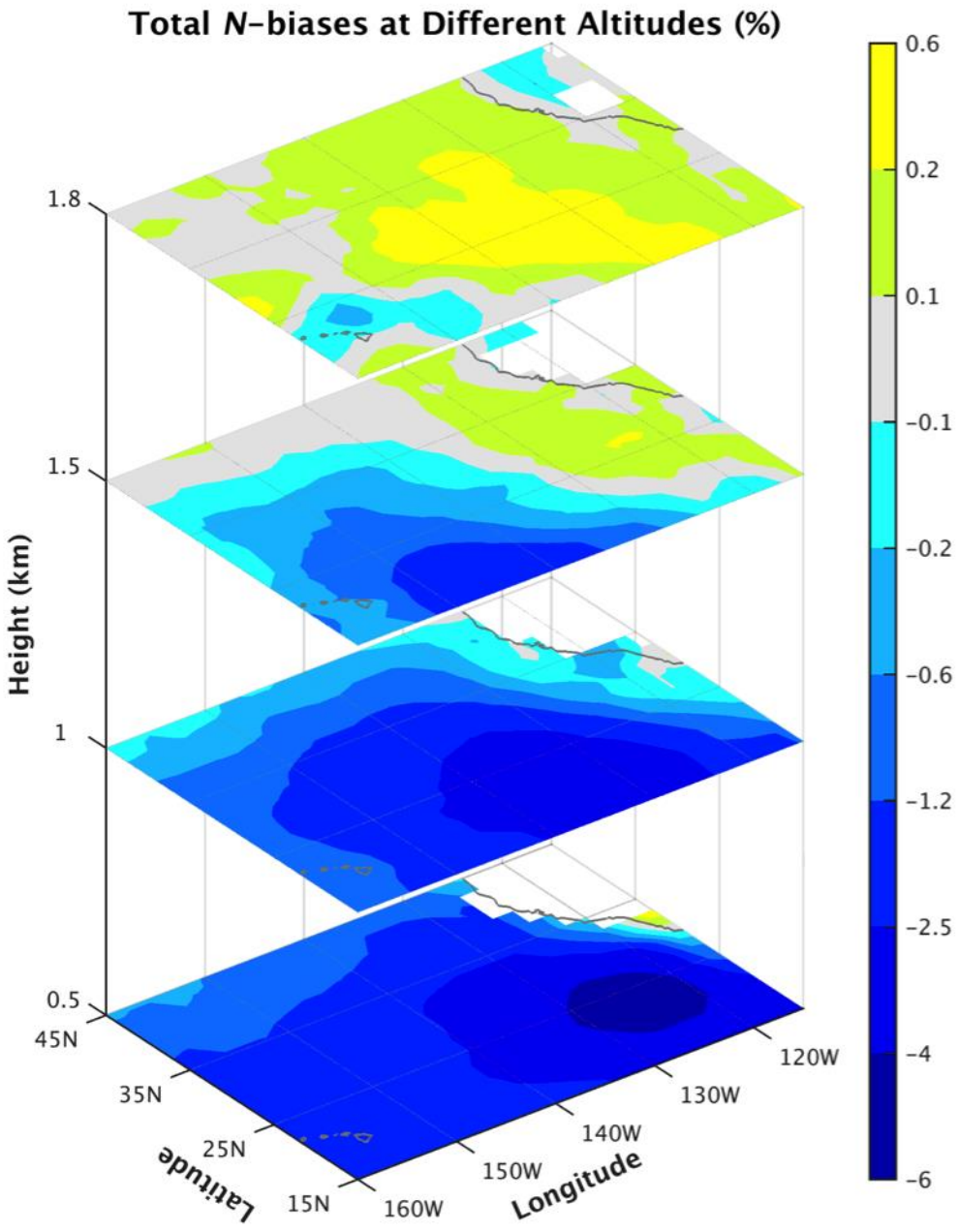

380

381 Figure 7. COSMIC RO *N*-bias $<(N_{COSMIC}-N_{ERAI})/N_{ERAI}>*100$ (%) with respect to ERA-I at 0.5-km,
382 1.0-km, 1.5-km, and 1.8-km above mean sea level.

383 Fig. 7 shows the fractional COSMIC *N*-biases with respect to ERA-I at four altitudes.
384 This *N*-bias pattern qualitatively resembles the bending angle bias pattern (Fig. 6). The
385 widespread negative *N*-bias center also gradually shifts from the ocean off the west coast
386 of southern California at 0.5-km southwestward to Hawaii at higher levels.

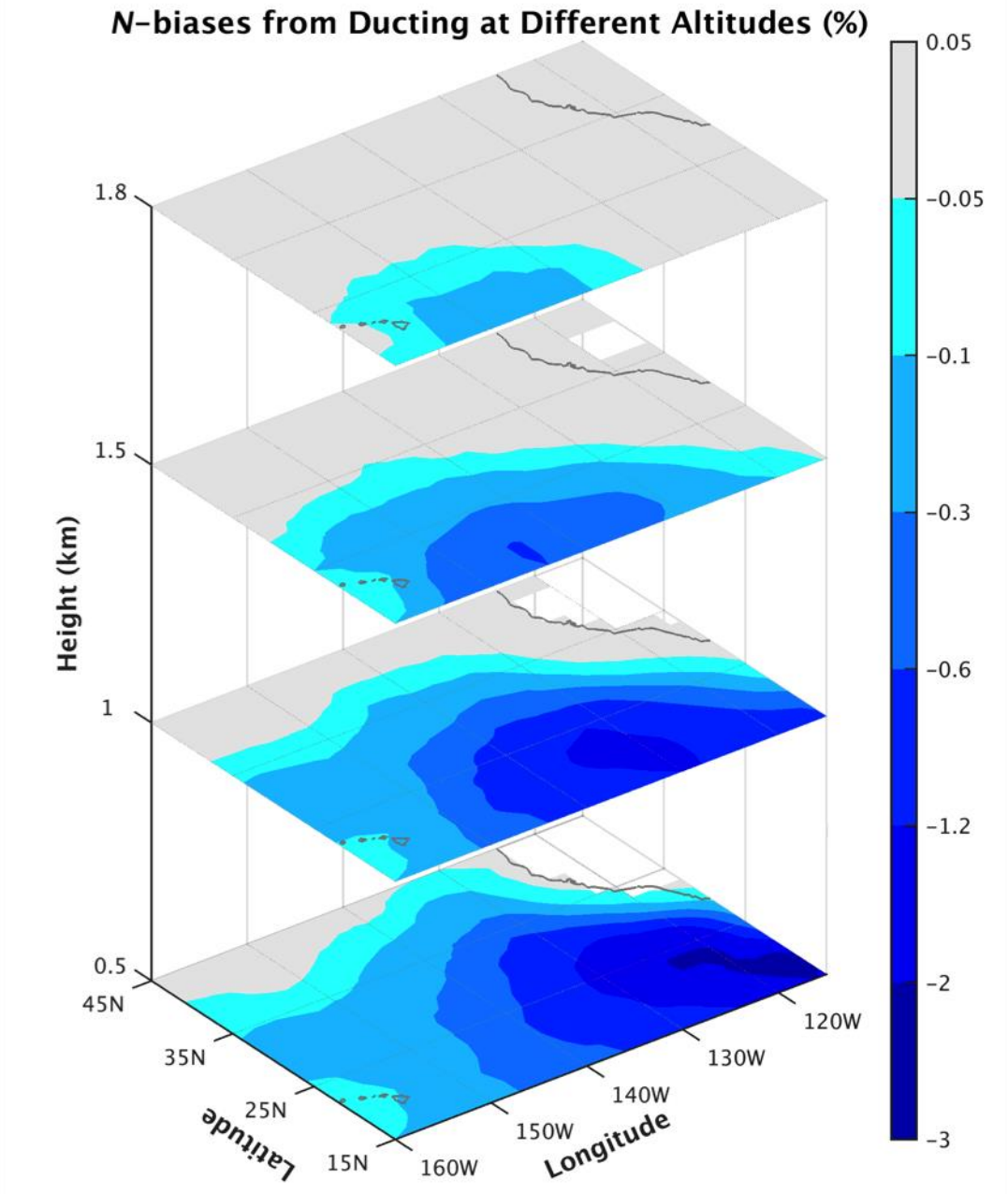

Figure 8. Simulated ducting-induced N-bias $<(N_{ERAI\text{-}simulated} - N_{ERA})/N_{ERA}>*100$ (%) at 0.5-km, 1.0-km, 1.5-km, and 1.8-km above mean sea level.

Next we quantify the fraction of the N-biases caused by ducting based on the ERA-I data. The bending angle profiles are first simulated given the input refractivity field from ERA-I (N_{ERAI}), and then the simulated RO refractivity ($N_{ERAI\text{-}simulated}$) are derived. In the presence of a ducting layer in ERA-I, the simulated refractivity retrieval will be

negatively biased to the N_{ERAI}, and the simulated *N*-biases represent the ducting-caused *N*-biases. Figure 8 shows the fractional *N*-biases in the ERA-I caused by ducting $<(N_{ERAI\text{-}simulated} - N_{ERAI})/N_{ERAI} \times 100>$. In comparison to the total COSMIC *N*-biases (Fig. 7), the ducting-induced *N*-biases share very similar pattern but with reduced magnitude.

The difference between the total and the ducting-induced *N*-biases, i.e., the residual *N*-biases, is shown in Fig. 9. In addition to those associated with ducting, negative biases in bending angles and refractivity may also be caused by errors associated with low SNR in the complex moist lower troposphere (Sokolovskiy, 2003; Beyerle et al., 2003; Kuo et al., 2004). Complicated refractivity structures in the lower troposphere result in rays (sub-signals) with large bending angles and low amplitudes. These sub-signals cannot be resolved against the background noise and the RO signal must be truncated, preferentially removing sub-signals with large bending angles from the inversion and resulting in a negative bias in bending angles and refractivity (Sokolovskiy et al., 2010). The underestimation of bending angles due to these effects has also been observed in airborne RO measurements (Wang et al., 2016).

Another potential source of negative bias is related to the propagation of radio waves in a medium with random refractivity irregularities. This nonlinear effect can be explained by Fermat's principle that a wave always takes the trajectory with the minimum phase path, which, on the average, is smaller than the phase path in the averaged refractivity (Eshleman and Haugstad, 1977). However, this simple explanation (i) does not account for multipath propagation and (ii) the absolute phase is not an observable. Gorbunov et al. (2015) demonstrated that this effect, in combination with vertically changing strength of irregularities and mean refractivity, results in a negative bias of refractivity retrieved from bending angle derived from the Doppler shift, the main RO observable. It may be possible that the bias due to random refractivity irregularities is dominant in the moist convective troposphere.

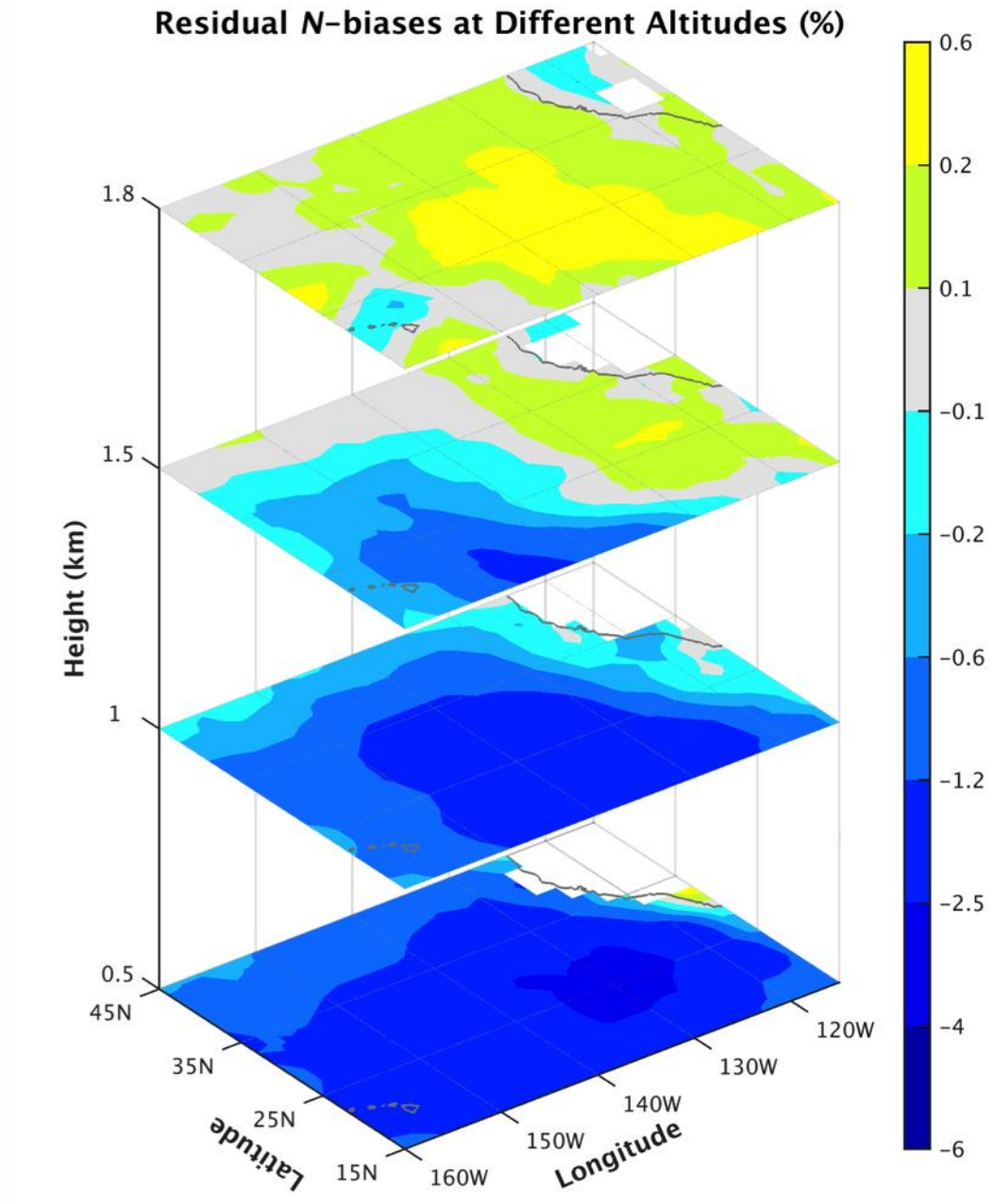

420

421 Figure 9. Difference (%) between observed COSMIC RO *N*-biases (Fig. 7) and ducting-induced
422 *N*-biases in the ERA-I data set (Fig. 8) at 0.5-km, 1.0-km, 1.5-km, and 1.8-km above mean sea
423 level.

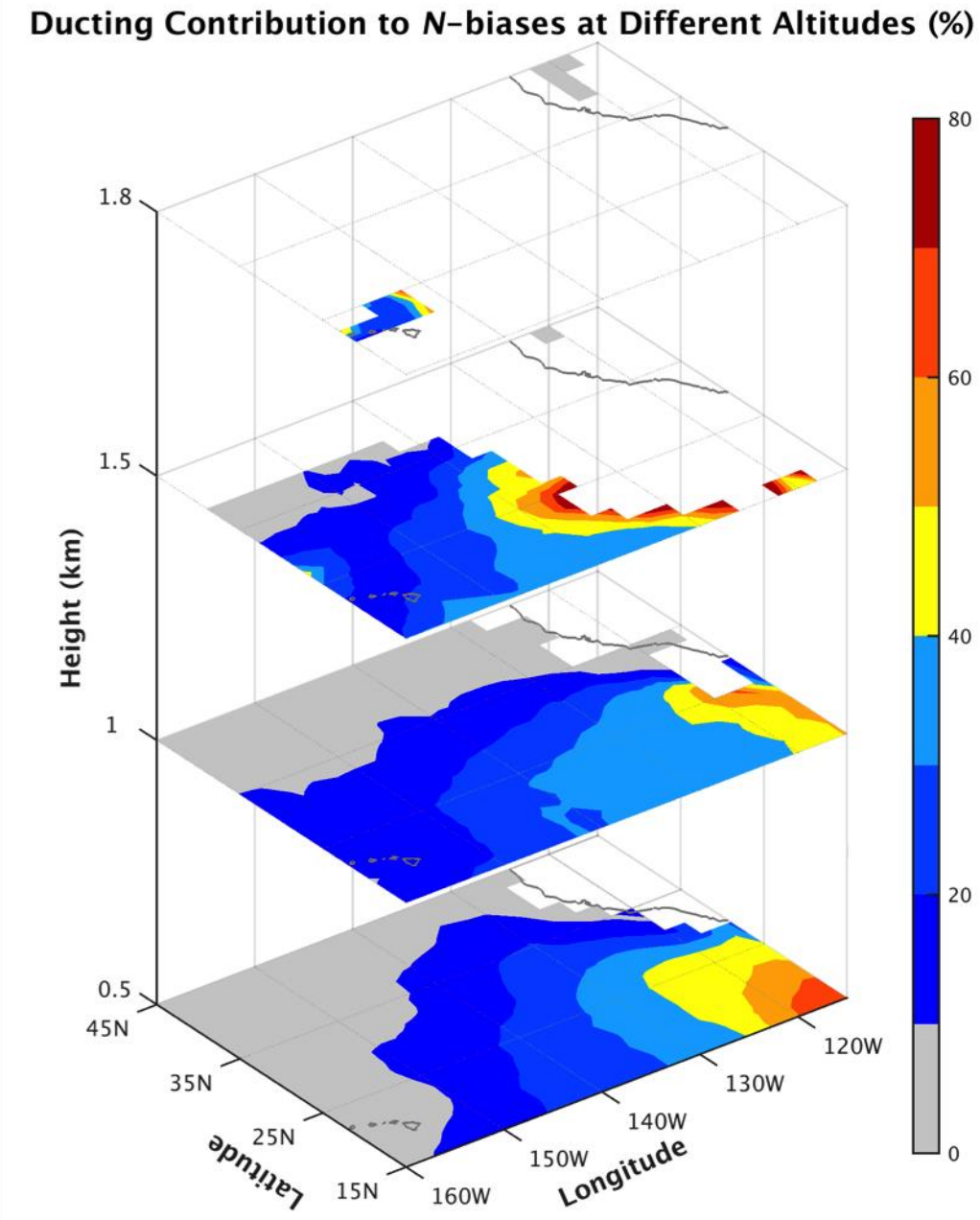

424

425 Figure 10. The ratio (%) of the magnitudes of the ducting-induced fractional *N*-biases (Fig. 8) to
426 the observed COSMIC *N*-biases (Fig. 7) at 0.5, 1.0, 1.5 and 1.8-km above mean sea level.

427 The fractional contribution of ducting-induced *N*-biases (from Fig. 8) to the total negative
428 *N*-biases (from Fig. 7) is shown in Fig. 10. The regions where the total *N*-bias is positive
429 and where the fraction is greater than 1 at 1.5-km and 1.8-km (Fig. 7) are blocked. The
430 largest percentages are concentrated on the southeast corner of this domain where the

ducting prevails (Fig. 1c), and the extreme values may exceed 50%. This indicates that ducting is the major cause of *N*-biases in the ducting prevailing region. For the full study region, ducting accounts for ~25% of the total *N*-biases at both the 0.5-km and 1.0-km levels. However, the ducting-induced *N*-biases derived from ERA-I could be underestimated due to the relatively coarse ERA-I vertical resolution. Therefore, the 25% area averaged *N*-biases due to ducting may be underestimated.

5 Summary

Using 8-years (2006-2013) of COSMIC RO soundings and ERA-I reanalysis data, we have investigated the climatology and seasonality of the global ducting distributions and of the global COSMIC RO *N*-biases distributions in comparison to ERA-I in the lower troposphere.

The systematically negative *N*-biases from RO soundings are confined to the lower troposphere over lower latitudes. The *N*-biases prevail below ~2-km, with the maximum magnitude of up to ~6%. Small positive *N*-biases above 2-km over tropics are also found. Over the oceans, large negative *N*-biases cluster over the subtropical oceans near the west coast of the continents. The magnitudes of *N*-biases are larger over oceans than over land, but their seasonality over land is larger than over oceans. The significant *N*-biases over land are mainly seen in regions of the complex topography, and seem not to be caused by ducting.

The bending angles of ERA-I and MAGIC radiosondes are simulated using the forward Abel integration in the northeast Pacific domain (160°W~110°W; 15°N~45°N). In this domain, systematically negative bending angle biases in COSMIC RO soundings with respect to collocated ERA-I data are found. Simulated bending angle profiles from MAGIC radiosondes confirm the existence and the magnitude of the RO bending angle biases. Significant negative bending angle biases are present below ~2-km with the peak biases at ~1-km above the surface, while the negative *N*-biases in this region peak at ~0.5-km. The locations of both the maximum biases in bending angles and refractivity tilt from northeast to southwest, following the increase of PBL height from less than 1-km offshore of southern California to about 1.8-km near Hawaii.

Moreover, the ducting-induced *N*-biases simulated from ERA-I data are calculated in the northeast Pacific domain. Although with a smaller magnitude, it shows a similar distribution pattern to the observed total COSMIC *N*-biases, and confirms the importance of ducting to the observed negative RO biases. In regions with prevailing ducting, over 50% of *N*-biases can be attributed to the ducting. Likely reasons for the non-ducting induced negative refractivity and bending angle biases are retrieval errors in the complex lower moist troposphere under low SNR conditions. The recently-launched COSMIC follow-on mission, COSMIC-2/FORMOSAT-7, is expected to have more than twice the SNR of COSMIC, and could have significantly lower bending angle biases than COSMIC. Other reasons may be related to the Fermat principle in which radio waves always take the path with the minimum integrated phase in an inhomogeneous medium. The underestimation of ducting-induced *N*-biases in the ERA-I analysis may also contribute to the apparent RO biases.

Acknowledgements X. Feng and F. Xie are supported by the NASA grant (NNX15AQ17G). The COSMIC RO soundings were provided by the Jet Propulsion Laboratory (JPL). Work performed by C. Ao was carried out at the JPL, California Institute of Technology, under a contract with the National Aeronautics and Space Administration. R. Anthes was supported by NSF-NASA Grant AGS-1522830. The high-resolution ECMWF analysis data were acquired from ECMWF. The MAGIC deployment was supported by the U.S. Department of Energy (DOE) Atmospheric Radiation Measurement (ARM) Program Climate Research Facility. We thank Sergey Sokolovskiy for his helpful comments on the causes of the RO biases. The support of Eric DeWeaver and Jack Kaye is also greatly appreciated.

References

Adhikari, L., F. Xie, and J. S. Haase (2016), Application of the full spectrum inversion algorithm to simulated airborne GPS radio occultation signals, *Atmos. Meas. Tech*., **9**, 5077-5087, doi:10.5194/amt-9-5077-2016.

Anthes, R. A., P. A. Bernhardt, Y. Chen, L. Cucurull, K. F. Dymond, D. Ector, S. B. Healy, S. P. Ho, D. C. Hunt, Y.-H. Kuo, H. Liu, K. Manning, C. McCormick, T. K. Meehan, W. J. Randel, C. Rocken, W. S. Schreiner, S. V. Sokolovskiy, S. Syndergaard, D. C. Thompson, K. E. Trenberth, T. K. Wee, N. L. Yen, and Z. Zeng (2008), The COSMIC/FORMOSAT-3 Mission: Early results. *Bull. Amer. Meteor. Soc*., **89**, 313–333.

Anthes, R. A. (2011), Exploring Earth's atmosphere with radio occultation: contributions to weather, climate and space weather, *Atmos. Meas. Tech.*, **4**, 1077-1103, doi:10.5194/amt-4-1077-2011.

Ao, C. O., T. K. Meehan, G. A. Hajj, A. J. Mannucci, and G. Beyerle (2003), Lower troposphere refractivity bias in GPS occultation retrievals, *J. Geophys. Res.*, **108**(D18), 4577, doi:10.1029/2002JD003216.

Ao, C. O., (2007), Effect of ducting on radio occultation measurements: An assessment based on high-resolution radiosonde soundings. *Radio Sci.*, **42**, RS2008.

Ao, C. O., S. K. Chan, B. A. Iijima, J.-L. Li, A. J. Mannucci, J. Teixeira, B. Tian, and D. E. Waliser (2008), Planetary boundary layer information from GPS radio occultation measurements, paper presented at ECMWF GRAS SAF Workshop on Applications of GPS Radio Occultation Measurements, ECMWF, Reading, U. K.

Ao, C. O., and coauthors (2009), Rising and setting GPS occultations by use of open-loop tracking, *J. Geophys. Res.*, **114**, D04101, doi:10.1029/2008JD010483.

Ao, C. O., D. E. Waliser, S. K. Chan, J.-L. Li, B. Tian, F. Xie, and A. J. Mannucci (2012), Planetary boundary layer depths from GPS radio occultation profiles, *J. Geophys. Res*., **117**, D16117, doi:10.1029/2012JD017598.

Basha, G., and M. V. Ratnam (2009), Identification of atmospheric boundary layer height over a tropical station using high-resolution radiosonde refractivity profiles: Comparison with GPS radio occultation measurements, *J. Geophys. Res.,* 114, D16101.

513 Beyerle, G., M. E. Gorbunov, and C. O. Ao (2003), Simulation studies of GPS radio
514 occultation measurements, *Radio Sci*., **38**(5), 1084, doi:10.1029/2002RS002800.

515 Beyerle, G., T. Schmidt, J. Wickert, S. Heise, M. Rothacher, G. Konig-Langlo, and K. B.
516 Lauritsen (2006), Observations and simulations of receiver-induced refractivity biases in
517 GPS radio occultation. *J. Geophys. Res.*, **111**, D12101.

518 Bonafoni, S., R. Biondi, H. Brenot, and R. Anthes (2019), Radio occultation and ground-
519 based GNSS products for observing, understanding and predicting extreme events: a
520 review. *Atmos. Research*, **230**, 1-18 https://doi.org/10.1016/j.atmosres.2019.104624

521 Born, M., and E. Wolf (1964), Principles of Optics: Electromagnetic Theory of
522 Propagation, Interference and Diffraction of Light. Pergamon Press, 856 pp.

523 Cucurull, L., and J. C. Derber (2008), Operational implementation of COSMIC
524 observations into NCEP's Global Data Assimilation System, *Weather Forecast*., **23**, 702–
525 711.

526 Cheng, C.-Z., Y.-H. Kuo, R. A. Anthes, and L. Wu (2006), Satellite constellation
527 monitors global and space weather. *Eos, Trans. Amer. Geophys. Union*, **87**, 166 –167.

528 Dee, D. P, and Coauthors (2011), The ERA-Interim reanalysis: configuration and
529 performance of the data assimilation system, *Q. J. R. Meteorol. Soc.*, **137**, 553–597.

530 Eshleman, V. R., and B. S. Haugstad (1977), Lowest-order average effect of turbulence
531 on atmospheric profiles derived from radio occultation, *Astrophys. J*., **214**(3), 928–933,
532 doi:10.1086/155325.

533 Feng, D. D., and B. M. Herman (1999), Remotely sensing the Earth's atmosphere using
534 the Global Positioning System (GPS), the GPS/MET data analysis, *J. Atmos. Oceanic.*
535 *Technol.*, **16**, 989-1002.

536 Fischbach, F. F. (1965), A satellite method for pressure and temperature below 24 km.
537 *Bull. Am. Meteor. Soc*., **46**:528-532

538 Fjeldbo, G., A. J. Kliore, and V. R. Eshleman (1971), The neutral atmosphere of Venus
539 as studied with the Mariner V radio occultation experiment. *Astron. J.*, **76**, 123–140.

540 Gorbunov, M. E., and A. S. Gurvich (1998), Microlab-1 experiment: Multipath effects in
541 the lower troposphere, *J. Geophys. Res.*, **103**, 13,819– 13,826.

542 Gorbunov, M. E. (2002a), Canonical transform method for processing radio occultation
543 data in the lower troposphere, *Radio Sci.*, **37**(5), 1076, doi:10.1029/2000RS002592.

544 Gorbunov, M. E. (2002b), Radio-holographic analysis of Microlab-1 radio occultation
545 data in the lower troposphere, *J. Geophys. Res.*, **107**(D12), 4156,
546 doi:10.1029/2001JD000889.

547 Gorbunov, M. E., H. H. Benzon, A. S. Jensen, M. S. Lohmann, and A. S. Nielsen (2004),
548 Comparative analysis of radio occultation processing approaches based on Fourier
549 integral operators, *Radio Sci.*, **39**, RS6004.

550 Gorbunov, M. E., V. V. Vorob'ev, and K. B. Lauritsen (2015), Fluctuations of
551 refractivity as a systematic error source in radio occultations, *Radio Sci*., **50**, 656–669.

552 Guo, P., Y.-H. Kuo, S. Sokolovskiy, and D. H. Lenschow (2011), Estimating
553 atmospheric boundary layer depth using COSMIC radio occultation data, *J. Atmos. Sci.*,
554 **68**, 1703– 1713.

555 Hajj, G. A., E. R. Kursinski, L. J. Romans, W. I. Bertiger, and S. S. Leroy (2002), A
556 technical description of atmospheric sounding by GPS occultation, J. Atmos. *Sol.-Terr.*
557 *Phys.*, **64** (4), 451–469.

558 Healy, S. B. (2001), Radio occultation bending angle and impact parameter errors caused
559 by horizontal refractive index gradients in the troposphere: A simulation study. *J.*
560 *Geophys. Res.*, **106,** 11875–11889.

561 Healy, S. B., and J.-N. Thépaut (2006), Assimilation experiments with CHAMP GPS
562 radio occultation measurements. *Quart. J. Roy. Meteor. Soc.*, **132**, 605–623.

563 Healy, S. B., (2008), Forecast impact experiment with a constellation of GPS radio
564 occultation receivers. *Atmos. Sci. Lett.*, **9,** 111–118.

565 Ho, S. -P., G. Kirchengast, S. Leroy, J. Wickert, A. J. Mannucci, A. Steiner, D. Hunt, W.
566 Schreiner, S. Sokolovskiy, C. O. AO, M. Borsche, A. von Engeln, U. Foelsche, S. Heise,
567 B. Iijima, Y. H. Kuo, R. Kursinski, B. Pirscher, M. Ringer, C. Rocken, and T. Schmidt
568 (2009), Estimating the uncertainty of using GPS RO data for climate monitoring: Inter-
569 comparison of CHAMP refractivity climate records 2002–2006 from different data
570 centers, *J. Geophys. Res.*, **114**, D23107.

571 Ho, S.-P, L. Peng, R. A. Anthes, Y.-H. Kuo, and H.-C. Lin (2015), Marine Boundary
572 Layer Heights and their Longitudinal, Diurnal and Inter-seasonal Variability in the
573 Southeast Pacific using COSMIC, CALIOP, and Radiosonde Data. *J. Climate*, **28,** 2856-
574 2872. https://doi.org/10.1175/JCLI-D-14-00238.1

575 Ho, S.-P., R. A. Anthes, C. O. Ao, S. Healy, A. Horanyi, D. Hunt, A. J. Mannucci, N.
576 Pedatella, W. J. Randel, A. Simmons, A. Steiner, F. Xie, X. Yue, and Z. Zeng (2019),
577 The COSMIC-FORMOSAT-3 radio occultation mission after 12 years:
578 accomplishments, remaining challenges, and potential impacts of COSMIC-2. *Bull. Am.*
579 *Meteorol. Soc.* 100, 2019 (in review).

580 Jensen, A. S., M. S. Lohmann, H.-H. Benzon, and A. S. Nielsen (2003), Full Spectrum
581 Inversion of radio occultation signals, *Radio Science*, **38**(3), 1040.

582 Jensen, A. S., M. S. Lohmann, A. S. Nielsen, and H.-H. Benzon (2004), Geometrical
583 optics phase matching of radio occultation signals, *Radio Science*, **39**, RS3009.

584 Kalmus P., S. Wong, and J. Teixeira (2015), The Pacific Subtropical Cloud Transition: A
585 MAGIC Assessment of AIRS and ECMWF Thermodynamic Structure, *IEEE Geosci.*
586 *Remote S.*, **12**, 1586–1590, doi:10.1109/LGRS.2015.2413771.

587 Kuo, Y.-H., T.-K. Wee, S. Sokolovskiy, C. Rocken, W. Schreiner, D. Hunt, and R. A.
588 Anthes (2004), Inversion and error estimation of GPS radio occultation data. *J. Meteor.*
589 *Soc. Japan*, **82**, 507–531.

590 Kursinski, E. R., G. A. Hajj, J. T. Schofield, R. P. Linfield, and K. R. Hardy (1997),
591 Observing Earth's atmosphere with radio occultation measurements using the Global
592 Positioning System. *J. Geophys. Res.*, **102**, 23429–23465.

593 Kursinski, E. R., G. A. Hajj, S. S. Leroy, and B. M. Herman (2000), The GPS radio
594 occultation technique, *Terr. Atmos. Oceanic Sci.*, **11**(1), 235–272.

595 Lopez, P., (2009), A 5-yr 40-km-resolution global climatology of superrefraction for
596 ground-based weather radars. *J. Appl. Meteor. Climatol.*, **48**, 89–110.

597 Luntama, J.-P., G. Kirchengast, M. Borsche, U. Foelsche, A. Steiner, S. Healy, A. von
598 Engeln, E. O'Clerigh, and C. Marquardt (2008), Prospects of the EPS GRAS Mission
599 for Operational Atmospheric Applications. *Bull. Amer. Meteor. Soc.*, **89**, 1863–1875.

600 Lusignan, B., G. Modrell, A. Morrison, J. Pomalaza, and S. Ungar (1969), Sensing the
601 earth's atmosphere with occulting satellites. *Proc. IEEE*, **4,** 458–467.

602 Poli, P., S. B. Healy, and D. P. Dee (2010), Assimilation of Global Positioning System
603 radio occultation data in the ECMWF ERA-Interim reanalysis. *Q. J. R. Meteorol. Soc.*,
604 **136**, 1972–1990.

605 Rocken, C., R., and Coauthors (1997), Analysis and validation of GPS/MET data in the
606 neutral atmosphere. *J. Geophys. Res*., **102** (D25), 29 849–29 866.

607 Smith, E. K., and S. Weintraub (1953), The constants in the equation for atmospheric
608 refractive index at radio frequencies. *Proc. IRE*, **41**, 1035–1037.

609 Sokolovskiy, S. (2003), Effect of superrefraction on inversions of radio occultation
610 signals in the lower troposphere, *Radio Sci.*, **38**, 1058, doi:10.1029/2002RS002728.

611 Sokolovskiy, S., Y.-H. Kuo, C. Rocken, W. S. Schreiner, D. Hunt, and R. A. Anthes
612 (2006), Monitoring the atmospheric boundary layer by GPS radio occultation signals
613 recorded in the open-loop mode, *Geophys. Res. Lett.*, **33**, L12813.

614 Sokolovskiy, S. V., C. Rocken, D. H. Lenschow, Y.-H. Kuo, R. A. Anthes, W. S.
615 Schreiner, and D. Hunt (2007), Observing the moist troposphere with radio occultation
616 signals from COSMIC, *Geophys. Res. Lett.*, **34**, L18802.

617 Sokolovskiy, S., C. Rocken, W. Schreiner, and D. Hunt (2010), On the uncertainty of
618 radio occultation inversions in the lower troposphere, *J. Geophys. Res.*, **115**, D22111,
619 doi:10.1029/2010JD014058.

620 Tsuda, T., Nishida N., Rocken C. and R. Ware (2000), A global morphology of gravity
621 wave activity in the stratosphere revealed by the GPS occultation data (GPS/MET), *J.*
622 *Geophys. Res*. **105**, 7257-7273.

623 Thomas, M. E., (2006), Optical propagation in linear media: atmospheric gases and
624 particles, solid state components, and water. Oxford [Oxfordshire]: Oxford University
625 Press. pp. 327–328. ISBN 0-19-509161-2.

626 von Engeln, A., and J. Teixeira (2004), A ducting climatology derived from the European
627 Centre for Medium-Range Weather Forecasts global analysis fields. *J. Geophys. Res.*,
628 **109**, D18104.

629 Wang, K.-N., J. L.Garrison, U. Acikoz, J. S. Haase, B. J. Murphy, P. Muradyan, T.
630 Lulich (2016), Open-loop tracking of rising and setting GPS radio-occultation signals
631 from an airborne platform: Signal model and error analysis. *IEEE Transactions on*

Geoscience and Remote Sensing. **54**, 3967-3984. https://doi.org/10.1109/TGRS.2016.2532346

Wang, K.-N., M. de la Torre Juarez, C. O. Ao, and F. Xie (2017), Correcting negatively-biased refractivity below ducts in GNSS radio occultation: An optimal estimation approach towards improving planetary boundary layer (PBL) characterization, *Atmos. Meas. Tech.*, 10, 4761–4776, https://doi.org/10.5194/amt-10-4761-2017.

Ware, R., and Coauthors (1996) GPS sounding the atmosphere from low earth orbit: Preliminary results. *Bull. Amer. Meteor. Soc.*, **77,** 19–40.

Ware, R., C. Rocken, F. Solheim, M. Exner, W. Schreiner, R. Anthes, D. Feng, B. Herman, M. Gorbunov, S. Sokolovskiy, K. Hardy, Y. Kuo, X. Zou, K. Trenberth, T. Meehan, W. Melbourne, and S. Businger (1996), GPS sounding of the Atmosphere from Low Earth Orbit; Preliminary Results, *Bull. Amer. Meteor. Soc*., **77**, 19-40, doi:10.1175/1520-0447i(1996).

Wickert, J., C. Reigber, G. Beyerle, R. König, C. Marquardt, T. Schmidt, L. Grunwaldt, R. Galas, T. Meehan, W. Melbourne, and K. Hocke (2001), Atmosphere sounding by GPS radio occultation: First results from CHAMP. *Geophys. Res. Lett.*, **28**, 3263-3266.

Xie, F. (2006) Development of a GPS occultation retrieval method for characterizing the marine boundary layer in the presence of super-refraction, Dissertation, University of Arizona, USA.

Xie, F., S. Syndergaard, E. R. Kursinski, and B. M. Herman (2006) An approach for retrieving marine boundary layer refractivity from GPS radio occultation data in the presence of super-refraction. *J. Atmos. Oceanic Technol.*, **23**, 1629–1644.

Xie, F., D. L. Wu, C. O. Ao, E. R. Kursinski, A. Mannucci and S. Syndergaard (2010) Super-refraction effects on GPS radio occultation refractivity in marine boundary layers, *Geophys. Res. Lett.*, **37**, L11805, doi:10.1029/2010GL043299.

Xie, F., D. L. Wu, C. O. Ao, A. J. Mannucci, and E. R. Kursinski (2012), Advances and limitations of atmospheric boundary layer observations with GPS occultation over southeast Pacific Ocean, *Atmos. Chem. Phys.*, **12**, 903-918.

Yu, X., F. Xie, and C. O. Ao (2018), Evaluating the lower-tropospheric COSMIC GPS radio occultation sounding quality over the Arctic, *Atmos. Meas. Tech.*, **11**, 2051-2066.

Yunck, T. P., G. F. Lindal, and C.-H. Liu (1988) The role of GPS in precise Earth observation, *IEEE Position Location and Navigation Symposium **(PLANS 88)***, 251–258.

Zeng, Z., S. Sokolovskiy, W. S. Schreiner, and D. Hunt (2019), Representation of vertical structures by radio occultation observations in the upper troposphere and lower stratosphere: Comparison to high-resolution radiosonde profiles. *J. Atmos. and Oceanic Tech.* https://doi.org/10.1175/JTECH-D-18-0105.1

Zheng, Y. and D. Rosenfeld (2015), Linear relation between convective cloud base height and updrafts and application to satellite retrievals. *Geophys. Res. Lett.*, **42**, 6485-6491, doi:10.1002/2015GL064809, 2015GL064809.

671 Zhou, X., P. Kollias, and E. Lewis (2015), Clouds, precipitation and marine boundary
672 layer structure during MAGIC, *J. Clim.*, **28**, 2420–2442, doi:10.1175/JCLI-D-14-
673 00320.1.